Physics of the Earth and Planetary Interiors 289 (2019) 106–114

Contents lists available at ScienceDirect

Physics of the Earth and Planetary Interiors

journal homepage: www.elsevier.com/locate/pepi

1D geothermal inversion of the lunar deep interior temperature and heat production in the equatorial area

Chengzi Jiang, Shuo Yao*

School of Geophysics and Information Technology, China University of Geosciences (Beijing), China

ARTICLE INFO

Keywords:
Lunar heat production
Lunar thermal state
Thermal conduction inversion

ABSTRACT

We present a study on lunar interior temperature and heat production by 1D geothermal inversion. With the layered structure and thermal state of the lunar interior reported by lunar seismic and magnetic sounding research, a forward modeling of deep temperature is given based on the theory of thermal conduction. Then, the particle swarm optimization (PSO) method is applied to implement the inversion of lunar interior heat production. A six-layer model is solved using a global heat flux of 12 mW/m^2 and a near-surface temperature of 250 K. The inversion results show that the crust has an average heat production of approximately 210 nW/m^3, the mantle has a depleted heat production varying from 3.7 to 8.1 nW/m^3, and the heat production in the lunar core varies from 30 to 36 nW/m^3. The distribution of heat production indicates that the present radioisotopes are mainly concentrated in the lunar crust. Different from previous estimates, the heat release in the lunar core may be considerable, similar to the average heat production in the Moon, implying that the residual heat from lunar accretion or radioactive decay is probably substantial; in contrast, perhaps the core was involved to a limit in the material exchange with the mantle. In addition, the obtained heat flux at the core-mantle boundary meets the value required for the core adiabatic process, indicating that the core convection may have stopped.

1. Introduction

In the 1970s, the Apollo missions investigated the lunar interior through the Apollo Lunar Surface Experiments Package (ALSEP), which contained a passive seismic experiment, active seismic experiment, lunar surface gravimeter, lunar surface magnetometer, and heat flow experiment. Both the passive seismic experiment and the lunar surface magnetometer were installed in the ALSEP of Apollo 12 and Apollo 15. The Apollo 12 landing site was close to the lunar equator, and that of Apollo 15 was at approximately 30 degrees north latitude. After processing the data measured by the passive seismic experiment, the moon was supposed to be composed of a crust, mantle, and core. In addition, shear wave attenuation indicates that the material was possibly melted below a depth of 1000 km. On the other hand, the variable magnetic field measured by the lunar surface magnetometer could reflect the electrical conductivity of the lunar interior. Together with the laboratory examinations of conductivity-temperature relationships for different minerals, the interior temperature was revealed from the electrical conductivity. Among the early studies, Sonett and Duba (1975), Sonett (1982), and Hood and Sonett (1982) reported the temperature constraints of the deep Moon based on the magnetic sounding measurements of the Apollo 12 near the equator. Langseth et al. (1976) presented a global heat flux of 18 mW/m^2 based on the measurements of the Apollo 15 and 17 heat-flow sites. Later, however, Warren and Rasmussen (1987) gave a revised global heat flux of 12 mW/m^2. The heat flow experiments of the Apollo 15 and 17 also revealed that the subsurface temperature was ~250 K at the heat flow sites and that the diurnal variation was negligible below about 80 cm (Langseth et al., 1976). Similarly, Vasavada et al. (1999) reported the stable near-surface temperature to be 250 K at the lunar equator using a 1-D two-layer thermal model.

Since the data analysis methods have greatly improved in the past twenty years, numerous researchers have reprocessed the Apollo data to better reveal the lunar interior. Lognonné et al. (2003) suggested a new lunar seismic model. Gagnepain-Beyneix et al. (2006) reported a seismic model of the lunar mantle and constraints on temperature and mineralogy, indicating the crustal thickness to be 30 km. Khan et al. (2004) and Weber et al. (2011) reanalyzed Apollo lunar seismograms, suggesting the presence of a solid inner and fluid outer core overlain by a partially molten layer. Later, Siegler and Smrekar (2014) used the Apollo heat flow data and a new three-dimensional thermal conduction model to examine effects of crustal thickness, density, and radioisotope abundance. They found that measured heat flux can be greatly altered by deep subsurface radiogenic content and crustal density. They also

* Corresponding author.
E-mail address: yaoshuo@cugb.edu.cn (S. Yao).

https://doi.org/10.1016/j.pepi.2019.02.007
Received 11 May 2018; Received in revised form 15 February 2019; Accepted 15 February 2019
Available online 23 February 2019
0031-9201/

reported an approximately 9–13 mW/m^2 mantle heat flux, which equals a total mantle heat production of 2.8–4.1 × 10^{11} W, being slightly less than earth's.

It is believed that the most important long-term heat source of the moon is the radioactive decay of uranium, thorium, and potassium. Abundances of these isotopes have been measured in returned lunar samples (LSPET, 1972, 1973; Clark and Keith, 1973; Tatsumoto et al., 1973), by lunar orbital gamma-ray spectrometers (Metzger et al., 1972), and by the surface gamma-ray experiment of Veneras 8, 9, and 10 (Keldysh, 1977). The global maps of uranium and thorium were obtained by the SELENE spacecraft (Yamashita et al., 2010). From Apollo lunar samples, the K/U ratios average approximately 2000, which is much lower than for terrestrial rocks. While the Th/U ratios are always between 3.0 and 4.0 for both terrestrial and lunar material (Toksöz et al., 1978). To match the measured heat flow value (Langseth et al., 1976), Toksöz et al. (1978) showed the bulk Uranium concentration must be approximately 35 ppb. It should be noted that the average radioactivity of the Moon is a function of the bulk Uranium content. It is expected that the magma is enriched in radioisotopes, transferring heat sources to the surface. Toksöz et al. (1978) suggested that the heat source may decrease exponentially with depth, leading to very small heat production values and Uranium contents in the cores of planets.

Since the lunar dynamo stopped long ago (Weiss and Tikoo, 2014; Wang et al., 2017), the lunar interior thermal state is critical evidence supporting the idea. This work aims to reveal the temperature and heat production of the lunar interior by one-dimensional geothermal inversion of the heat production based on the theory of thermal conduction. The thermal conduction equation, the boundary conditions and the inversion algorithm are introduced in Section 2. The results of inversion are shown in Section 3, followed by the discussion in Section 4 on the effects of changing parameters on the inversion results. The conclusions are drawn in the last section.

2. Modeling

2.1. Thermal conduction equation

According to Weber et al. (2011), the crust and the bulk of the mantle (0–1257 km) are solid. There is a partial melt layer at the bottom of the mantle (1257–1407 km), overlying the liquid outer core (1407–1497 km), while the inner core is solid with a radius of 240 km. On the other hand, palaeomagnetic study shows that the lunar dynamo has already stopped (Weiss and Tikoo, 2014), indicating that there is no significant convection in lunar core. Thus, the thermal conduction process is mainly considered in our model. The time-dependent thermal conduction equations derived from Wieczorek and Phillips (2000) are

$$\rho C_p \frac{\partial T}{\partial t} = A - \nabla \cdot \boldsymbol{q}, \tag{1}$$

and

$$\boldsymbol{q} = -\lambda \nabla T, \tag{2}$$

where ρ is the density, C_p is the specific heat at constant pressure, T is the temperature, A is the heat production per unit volume, $\boldsymbol{q}$ is the heat flux, and λ is the thermal conductivity.

We employ two assumptions for simplicity. First, the lunar model is spherically symmetric and is divided into several shells and one core. The properties in each shell are isotropic and homogeneous, and all parameters therefore vary only with radius (or depth). Second, since the moon has already cooled, the inner temperature is considered to be constant over time on a short time scale, and hence we have $\partial T/\partial t \approx 0$ in Eq. (1). Based on these two assumptions, the temperature can be solved:

$$T(r_1) = T_s + \int_0^R \frac{\int_0^r A(r) r^2 \mathrm{d}r}{\lambda(r) r^2} \mathrm{d}r - \int_0^{r_1} \frac{\int_0^r A(r) r^2 \mathrm{d}r}{\lambda(r) r^2} \mathrm{d}r, \quad 0 \le r_1 \le R, \tag{3}$$

where T_s is the subsurface temperature, r is the radius, A is the heat production per unit volume, λ is the thermal conductivity, and R is the radius of the moon. The detailed derivation of Eq. (3) and its discrete form are shown in the appendix.

Once the heat productions and thermal conductivities of all layers are given, we can determine the temperature profile of the moon from Eq. (3), which is the forward calculation in our model. To obtain heat production, we have to presume the deep temperature along with the conductivity of the lunar interior to solve the inverse problem of heat production.

2.2. Parameters in the model

In Eq. (3), there are two boundary conditions to determine: the near-surface temperature and the near-surface heat flux. For a one-dimensional quasi-static lunar model, the boundary conditions should not change with time. Vasavada et al. (1999) calculated the near-surface temperature on the Moon and obtained that diurnal mean temperature tends to be constant below 0.3 m depth. At the lunar equator, the mean subsurface temperature is approximately 250 K, which is used in our model as the value of temperature at 0 km depth. Langseth et al. (1976) presented a global heat flux of 18 mW/m^2. Later, Warren and Rasmussen (1987) revised the model and estimated that the global mean heat flux is 12 mW/m^2, which is used in our model as the value of heat flux at 0 km depth.

The near-surface heat flux constrains the total heat production of the lunar interior. For a layered lunar model, we have

$$\sum_{i=1}^{N} V_i A_i = 4\pi R^2 q_s, \tag{4}$$

where V_i is the volume of each shell, A_i is the heat production per unit volume, R is the radius of the Moon, and q_s is the global mean near-surface heat flux. Eq. (4) shows there is a linear constraint on the heat production of all layers, which has to be considered in the inversion calculation.

Moreover, in order to solve the inverse problem of heat production, the thermal conductivity of each layer has to be assumed. Branlund and Hofmeister (2012) measured the thermal conductivity of feldspars and gave values ranging from 1.5–1.9 W m^{-1} K^{-1}, changing little with temperature. Based on the previous assumption by Wieczorek and Phillips (2000) and Siegler and Smrekar (2014), we assume that the crust has an average thermal conductivity of 2 W m^{-1} K^{-1} and that the mantle has a conductivity of 3 W m^{-1} K^{-1}. The conductivity is not considered to change with temperature. It is still difficult to determine the thermal conductivity of the lunar core. According to Sanloup et al. (2000), the lunar core mainly consists of Fe-S alloy. In addition, Weber et al. (2011) estimated that the temperature in the lunar core is approximately 1500–1750 K, with the total content of sulfur in the core varying from 4 wt% to 8 wt%. Therefore, the core is assumed to have a high thermal conductivity of 10 W m^{-1} K^{-1} in our model so that our calculated temperature in the lunar core corresponds to the estimation of Weber et al. (2011). Although the estimation for the conductivity of the lunar core may have a large error, it actually has a limited effect on the temperature due to the low value of heat flux within the core.

2.3. Objective function

The basic idea of the inversion algorithm is to minimize the residual error between the calculated temperature and the reference temperature by modifying the layered model of heat production repeatedly.

With Eq. (3), a temperature curve can be calculated from a given

model of heat production and conductivity. Comparing this curve to the presumed reference temperature, we can obtain the RMSE of the fitting curve with the function

$$\varepsilon = \sqrt{\frac{1}{n}\sum_{i=1}^{n}(T_i - F_i)^2}, \tag{5}$$

where ε is the root-mean-square error, n is the number of reference points, T_i is the temperature calculated by Eq. (3), and F_i is the reference temperature obtained from the temperature profile of Hood and Sonett (1982).

Until recently, it is still impractical to directly measure the deep temperature of the Moon. Hence, we choose an indirect solution to determine the deep reference temperature. Hood and Sonett (1982) presented two temperature profiles calculated from the lunar electrical conductivity profile. The deep electrical conductivity is obtained from the magnetic sounding experiments (Sonett and Duba, 1975; Duba et al., 1976). Then, the deep temperature is calculated from electrical conductivity profiles with laboratory determined conductivity-temperature relationships (Duba et al., 1976). The temperature profiles presented in Hood and Sonett (1982) use two different conductivity-temperature relations for pyroxene in the lunar mantle: 1.9 wt% Al_2O_3 and 6.8 wt% Al_2O_3. We pick the medians between the higher and lower limits of temperature profile as the reference temperature in our model. In each profile, the medians are picked as reference points every 25 km in the range of 500–1300 km, so each profile derives 33 points (shown in Fig. 1), which are enough to obtain stable inversion results.

Every time a temperature curve is calculated, the layered model of heat production will be slightly modified based on the RMSE of calculated temperature to reduce the residual error of the new curve in the next iteration. After a large number of iterations, the model tends to be stable, and the residual error reaches a minimum. To accelerate the model convergence and to avoid the residual error being trapped in a local minimum, a suitable optimization algorithm is required in the inversion algorithm.

2.4. Particle swarm optimization

Particle swarm optimization (PSO) as proposed by Kennedy and Eberhart (1995) is applied in our inversion calculation. This algorithm uses a swarm of particles representing numerous random models to search for the global best model by fast iteration, which performs well in such a nonlinear inverse problem. Additionally, PSO is easily implemented in brief computer codes and requires a low memory footprint.

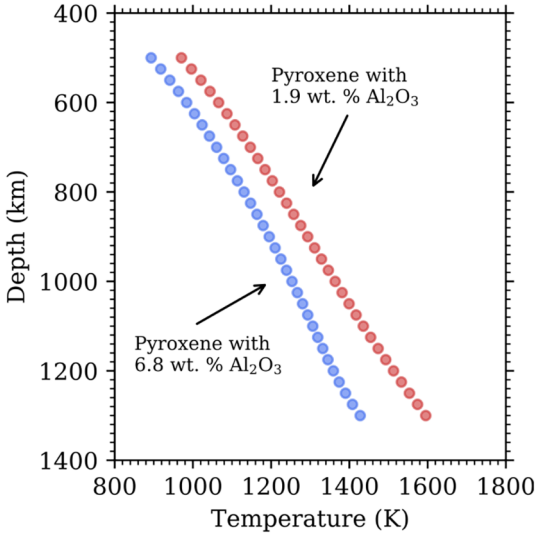

Fig. 1. The reference temperature points derived from the medians of the envelope of temperature profiles in Hood and Sonett (1982). The blue points are the medians of the profile using the conductivity-temperature relation for pyroxene with 6.8 wt% Al_2O_3, while the red points correspond to pyroxene with 1.9 wt% Al_2O_3. (For interpretation of the references to colour in this figure legend, the reader is referred to the web version of this article.)

The general ideas of PSO are as follows (Poli et al., 2007). First, initialize a large number of random particles in N-dimensional space. Each particle has its position $\vec{x_i}$ and velocity $\vec{v_i}$ on N dimensions. Each dimension represents one variable in the model to be solved. Second, calculate the fitness function for each particle with their current positions. The global best fitness among all particles is denoted *gbest*, and its position is denoted $\vec{p_g}$. The individual best fitness for each particle is called *pbest*, and their positions are defined as $\vec{p_i}$. Third, calculate a new velocity and new position for each particle with $\vec{p_g}$ and $\vec{p_i}$ by Eq. (6) (Clerc and Kennedy, 2002). Finally, finish the iteration if *gbest* meets the criterion or if the number of iterations meets the maximum; otherwise go to step two and repeat the iteration.

$$\begin{cases} \vec{v_i} \leftarrow 0.7298(\vec{v_i} + \vec{U}(0, 2.05) \otimes (\vec{p_i} - \vec{x_i}) + \vec{U}(0, 2.05) \otimes (\vec{p_g} - \vec{x_i})) \\ \vec{x_i} \leftarrow \vec{x_i} + \vec{v_i} \end{cases}, \tag{6}$$

where i is the ordinal number of particles, $\vec{v_i}$ and $\vec{x_i}$ are the velocity and position of the particle of order i, $\vec{p_i}$ is the individual best position of the particle of order i, $\vec{p_g}$ is the global best position for all particles, and $\vec{U}(0, 2.05)$ is a vector of random numbers uniformly distributed in [0, 2.05] with N dimensions. The vector $\vec{U}$ is randomly generated in each iteration, and $\otimes$ is the element-wise multiplication between the two vectors.

In the inversion calculation of heat production, the particle position in each dimension represents the heat production of each layer, hence an N-layer model corresponds to a particle with N dimensions. The particle velocity represents the slight change of heat production in each iteration. The fitness of each particle is the RMSE of calculated temperature. With the procedures presented in Poli et al. (2007), an inversion algorithm of heat production is implemented. The main procedures of the inverse algorithm are as follows.

(1) Initialize a position matrix of random particles (models) with a size of $P \times N$, where P is the particle number, the number of random models, and N is the layer number ($P = 1200$, and $N = 6$ in our model). The elements in the matrix are dimensionless heat production. The initial elements in the position matrix are randomly distributed in 0–1.
(2) Initialize a velocity matrix with the same size of $P \times N$ and set the initial dimensionless velocities of each particle randomly distributed in 0–1.
(3) Using Eq. (4), convert the dimensionless elements in the position matrix into the heat production and then calculate the temperature curve for each particle with Eq. (3).
(4) Calculate the RMSE of temperature curves with Eq. (5) as the fitness of particles.
(5) For each particle, if its current fitness is less than its individual best fitness (*pbest*), replace *pbest* and its corresponding position $\vec{p_i}$ with current values.
(6) For all particles, if the current best fitness is less than the global best fitness (*gbest*), replace *gbest* and its corresponding position $\vec{p_g}$ with current values.
(7) Calculate the velocities of all particles and their new positions with Eq. (6).
(8) If the maximum number of iterations is reached, go to the next step, and otherwise go to step (3).
(9) Output the best model of heat production and its RMSE of the temperature curves corresponding to $\vec{p_g}$ and *gbest*.

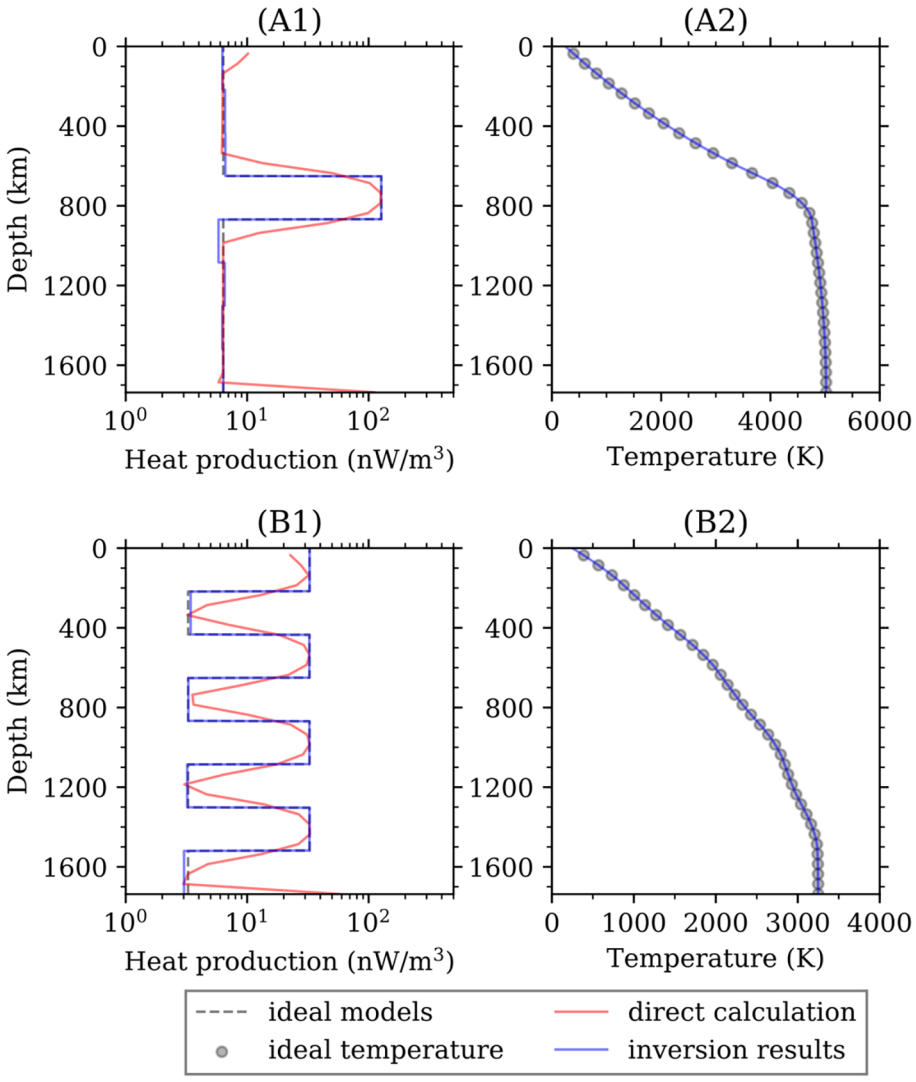

Fig. 2. Two test models for the inversion algorithm. (A1) An ideal model in which only one layer has a much higher value of heat production, while other layers have lower values. (A2) The temperature corresponding to the model in A1. (B1) An ideal model in which half of the layers have higher heat production, while the others have lower values. (B2) The temperature corresponding to the model in B1. The red lines in (A1) and (B1) are heat production directly calculated from the ideal temperature without using PSO. (For interpretation of the references to colour in this figure legend, the reader is referred to the web version of this article.)

2.5. Tests for the algorithm

As shown in Fig. 2, two tests for the inversion algorithm were conducted to inspect its reliability. The test models are two different artificial eight-layer models along with their calculated temperature curves. The first group is shown in (A1) and (A2), and the second group is shown in (B1) and (B2). Three thousand particles are used to solve these two models.

More particles, as well as more iterations, contribute to more stable results in the PSO, but also consume much more time. The result tends to converge to a local optimum if the particle number is not large enough. The specific numbers of particles and iterations depend on the dimension of the particle coordinates, which is also the layer number of the heat production in this problem. The inversion results shown in Fig. 2(A1) and (B1) are much closer to the ideal models compared with the direct calculation. With a sufficient quantity of particles, the results solved by PSO are considerably stable and robust. The mean relative error between the inversion results and the ideal model in Fig. 2 is less than 2%. Although the direct calculation of heat production using Eqs. (1) and (2) is continuous, it is actually rather sensitive to the refence temperature and is less reliable. Therefore, it is necessary to use the inversion algorithm to calculate the layered model of heat production.

3. Results

3.1. Six-layer models of the heat production

The inverted heat production is divided into a total of six layers shown in Fig. 3(A). The depth of the crust-mantle boundary (at a depth of 40 km) and core-mantle boundary (at a depth 1407 km) are based on the seismic inversion of Weber et al. (2011). The mantle is uniformly divided into four layers to reduce the fitting error of temperature. Since no reference temperature is available in the lunar core, the core is not divided into the inner and outer layers, and otherwise, the solution of heat production will not be convergent within the core.

As discussed in Section 2.2, the boundary conditions are the near-surface temperature, which is 250 K, and the global mean heat flux, which is 12 mW/m^2. Thermal conductivity is presumed to be 2 W m^{-1} K^{-1} in the crust, 3 W m^{-1} K^{-1} in the mantle and 10 W m^{-1} K^{-1} in the core. Using 1200 particles in PSO, two models of heat production are separately solved with two groups of reference temperature (Fig. 3).

Fig. 3(A) shows that the crust has the highest heat production (200 nW/m^3 for the higher reference temperature and 220 nW/m^3 for the lower reference temperature) among all six layers, while the heat production in mantle is much lower than that for the crust, with an

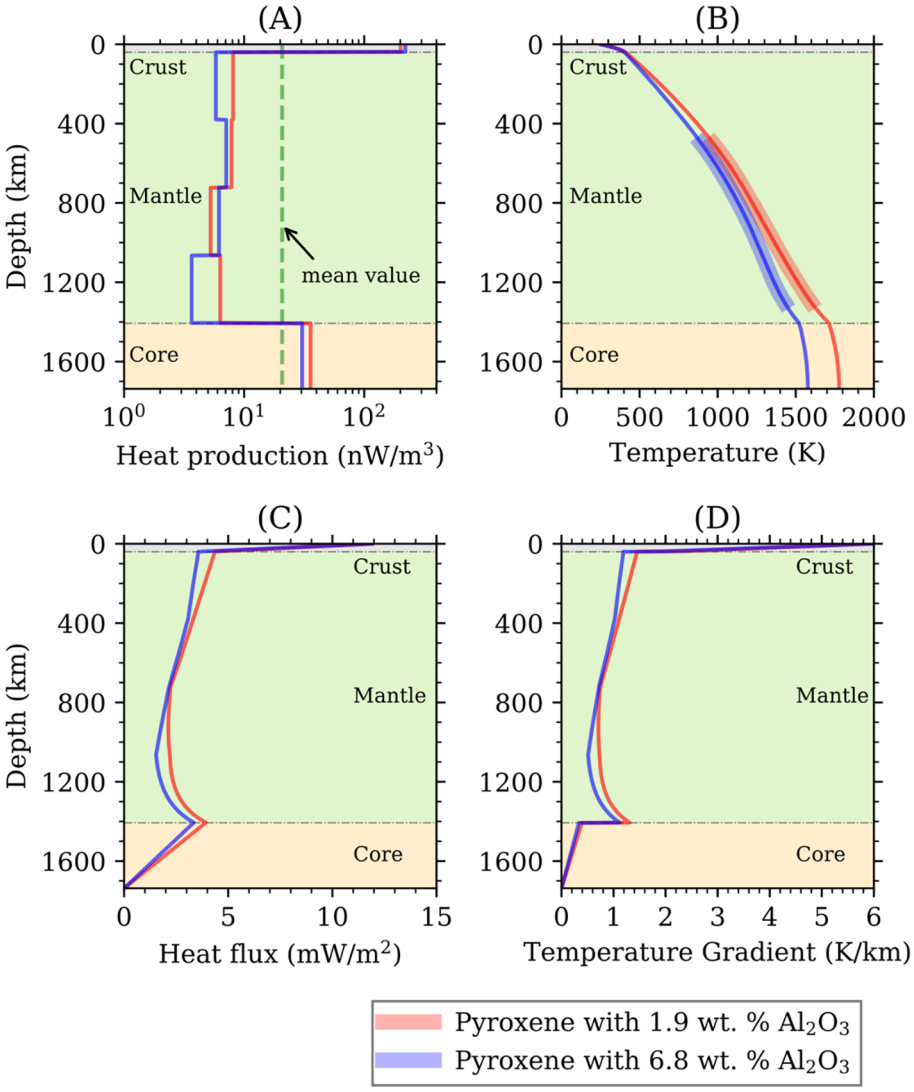

Fig. 3. The inversion results of lunar heat production and the corresponding forward responses. (A) Two sets of heat production obtained by inversion. The red line is calculated from the higher reference temperature, while the blue line is calculated from the lower reference temperature. The green dashed line is the mean heat production. (B) The calculated temperature curves. The red line fits the reference temperature in the red shade, corresponding to the temperature profile calculated with the mineral assumption for pyroxene with 1.9 wt% Al_2O_3 in Hood and Sonett (1982). Similarly, the blue shade of reference temperature corresponds to pyroxene with 6.8 wt% Al_2O_3. (C) The heat flux calculated with Eq. (2). (D) The temperature gradient calculated from the temperature curves in (B). (For interpretation of the references to colour in this figure legend, the reader is referred to the web version of this article.)

average value of ~6 nW/m^3. The heat production in the lunar core is 36 nW/m^3 for the higher reference temperature and 30 nW/m^3 for the lower reference temperature, between the values in the crust and mantle. In addition, the overall mean heat production (the green dashed line) is 20.7 nW/m^3. Obviously, the lunar mantle has a considerable depletion, while the crust has abundant heat production. It is interesting that heat production in the core is close to the mean value, which might suggest that the lunar core has limited material exchange with the mantle. In Fig. 3(B), the RMSEs between the calculated temperature and the reference temperature are ~0.7 K, so the results fit the reference temperature very well. The temperature at the crust-mantle boundary is 410 K on average. It is between 1522 K and 1712 K at the core-mantle boundary and increases slowly along depth within the core, ending up between 1578 K and 1778 K at the center of the Moon. The average temperature of the lunar core in our model accords with the estimation of Weber et al. (2011).

The heat flux in Fig. 3(C) decreases rapidly from 12 mW/m^2 to ~4 mW/m^2 in the lunar crust but varies little in the mantle. At the core-mantle boundary, the heat flux remains ~3.5 mW/m^2. Because of the low heat production in the whole mantle, there is no large difference between the heat flux at the crust-mantle boundary and that at the core-mantle boundary. The mantle heat flux calculated in our model is less than the assumed value in Siegler and Smrekar (2014) but agrees with that in Langseth et al. (1976).

The shape of the temperature gradient in Fig. 3(D) is similar to that of the heat flux. Its discontinuities on both the crust-mantle boundary and the core-mantle boundary result from the discontinuous thermal conductivities in different layers.

3.2. Estimating radioisotope abundance

High heat production in the lunar crust indicates a high radioisotope abundance, while low heat production in the mantle indicates a depleted radioisotope abundance (Langseth et al., 1976). However, the heat production in this model includes contributions from all kinds of underground heat sources. Two major heat sources are the heat from radioactive decay and the residual heat from lunar accretion. According to Turcotte and Schubert (2014), 20% of Earth's internal heat comes from planetary accretion, while the other 80% is mainly produced by the radioactive decay of ^{238}U, ^{232}Th and ^{40}K. Hence, we assume that the Moon has similar proportions with those of the Earth. In this case, the heat from radioisotope decay contributes to 80% of the calculated heat production, and the abundances of ^{238}U, ^{232}Th and ^{40}K can be calculated by Eq. (7) (Turcotte and Schubert, 2014; Warren and Wasson, 1979)

$$\begin{cases} \rho(94.6c_U + 26.4c_{Th} + 29.2c_K) \times 10^{-6} = A \times 80\% \\ c_U : c_{Th} : c_K = 1.0 : 3.7 : 1.1 \end{cases} \quad (7)$$

where ρ is the density of rocks (kg/m^3), c is the radioisotope abundance (ppb), and A is the heat production (nW/m^3).

Table 1
Radioisotope abundances calculated from the mean heat production in each layer of the two models.

Layer	Depth (km)	Density[a] (kg/m^3)	Mean heat production (nW/m^3)	^{238}U (ppb)	^{232}Th (ppb)	^{40}K (ppb)
Crust	0–40	2750	210	272.2	1007.3	299.5
Mantle	40–381	3340	7.0	7.5	27.6	8.2
	381–723	3350	7.5	8.0	29.5	8.8
	723–1065	3355	5.7	6.1	22.4	6.7
	1065–1407	3440	5.0	5.2	19.2	5.7
Core	1407–1737	5443	33.1	21.7	80.2	23.8

[a] Estimation from Weber et al. (2011).

The radioisotope abundances calculated by the heat production are listed in Table 1. Yamashita et al. (2010) presented a global map of uranium distribution and gave an average uranium abundance of ~300 ppb along with an average thorium abundance of ~1200 ppb. The abundances of uranium and thorium calculated in our model are 272.2 ppb and 1007.3 ppb, which are close to their observations.

4. Discussion

To discuss the effects of all the used parameters on the inverted results in our model, we change the value of the subsurface temperature, the heat flux, the thermal conductivity, and the internal temperature reference, separately. The corresponding results are shown in Fig. 4 and in Fig. 5. Three sets of comparisons with different near-surface temperatures, global heat fluxes and thermal conductivities are shown in Fig. 4(A)–(C), respectively. Two sets of comparisons with different deep temperature reference envelopes are shown in Fig. 5.

In Fig. 4, T_s and q_s are the near-surface temperature and the global mean heat flux, respectively. The normal conductivities are the values used in Section 3.1, which are 2 W m^{-1} K^{-1} in the crust, 3 W m^{-1} K^{-1} in the mantle and 10 W m^{-1} K^{-1} in the core. We took the subsurface temperature of 150 K obtained in polar region (Paige et al., 2010) to approximate the temperature without the influence of the long-term solar radiation. It should be noted that the variation of the subsurface temperature and the heat flux in Fig. 4 cannot be interpreted as the latitude variation, since all other parameters do not change.

According to Fig. 4(A) and (B), the changes in T_s and q_s both result in the change in heat production only at a depth from 0 to 381 km. With higher T_s or q_s, the heat production in the crust also increases, and it is more sensitive to the change in global heat flux than that in near-surface temperature. The trend is that lower subsurface temperature corresponds to lower heat production in crust but higher heat production in upper mantle, and the heat production in mantle is always much less than that in crust. With higher q_s the heat production in the crust increases, and it is more sensitive to the change in global heat flux than that in subsurface temperature. It is worth noting that the heat productions at a depth larger than 381 km have no response to the changes in T_s or q_s. This is because the calculated deep heat production is dominated by the deep reference temperature and the thermal conductivity, see Figs. 4(C) and 5.

In addition, with the 10% change in the thermal conductivity from the crust to the core, the inversion results of heat production change by approximately 10% as well in Fig. 4(C). Hence, the error of thermal conductivity has limited effect on the results.

Fig. 5 shows how the uncertainty of reference temperatures affects the calculated heat productions. Although there is a large difference between the higher and the lower limits of the temperature envelopes given by Hood and Sonett (1982), the uncertainty of the temperature is relatively small (approximately ±100 K) at the depth from 500 to 1300 km. Therefore, by using the median temperature values in this depth range, the uncertainty of these envelopes will have minimized influence on the inversion results. Fig. 5(A)–(C) show the results generated by different fitting curves of deep temperatures with the mineral assumption for pyroxene with 1.9 wt% Al_2O_3, while Fig. 5(D)–(F) are the other group of results with the assumption for pyroxene with 6.8 wt % Al_2O_3. The dashed lines and the dotted lines in all six subfigures represent the results of lower and higher temperature limits, respectively. Despite the reference temperature variations, the general trend of the heat production does not change that the largest value appears in crust and the smallest value appears in mantle. The heat production in mantle varies between ~0 and 9.6 nW/m^3 except for the upper mantle layer approaching 27.7 nW/m^3. The core tends to have a heat production of 17.2–61.4 nW/m^3. The largest uncertainty of the heat production occurs in the crust, varying between 89.3 and 266.0 nW/m^3. Therefore, compared with other parameters used in our model, the deep

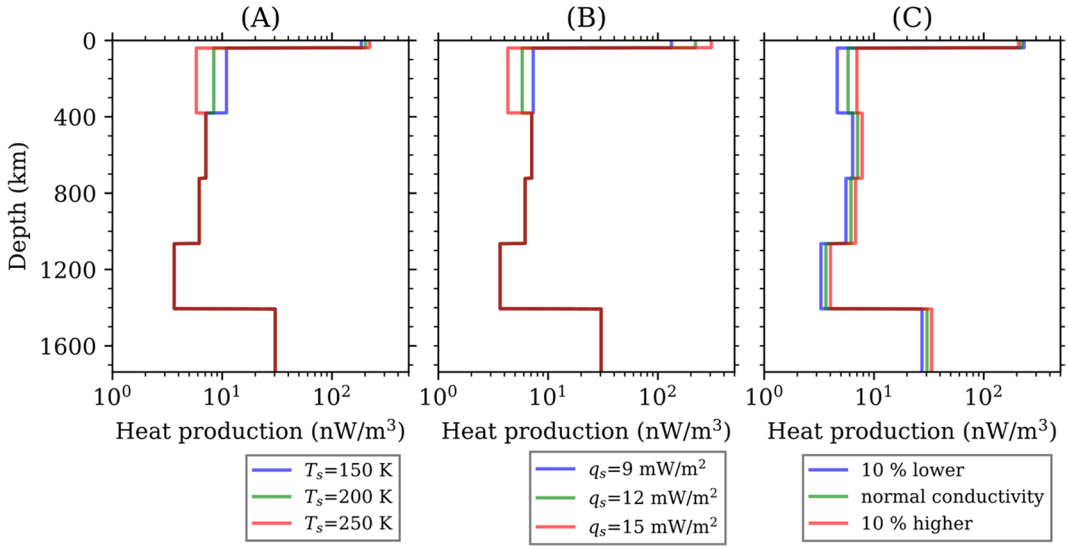

Fig. 4. The comparisons of inversion results with different subsurface temperatures, subsurface heat fluxes and thermal conductivities. (A) Using subsurface temperatures of 150 K (blue), 200 K (green) and 250 K (red) with q_s = 12 mW/m^2. (B) Using global heat fluxes of 9 mW/m^2 (blue), 12 mW/m^2 (green) and 15 mW/m^2 (red) with T_s = 250 K. (C) Using 10% lower (blue), 10% higher (red) and the normal thermal conductivities (green) used in Section 3.1, which are 2 W m^{-1} K^{-1} in the crust, 3 W m^{-1} K^{-1} in the mantle and 10 W m^{-1} K^{-1} in the core, along with T_s = 250 K and q_s = 12 mW/m^2. (For interpretation of the references to colour in this figure legend, the reader is referred to the web version of this article.)

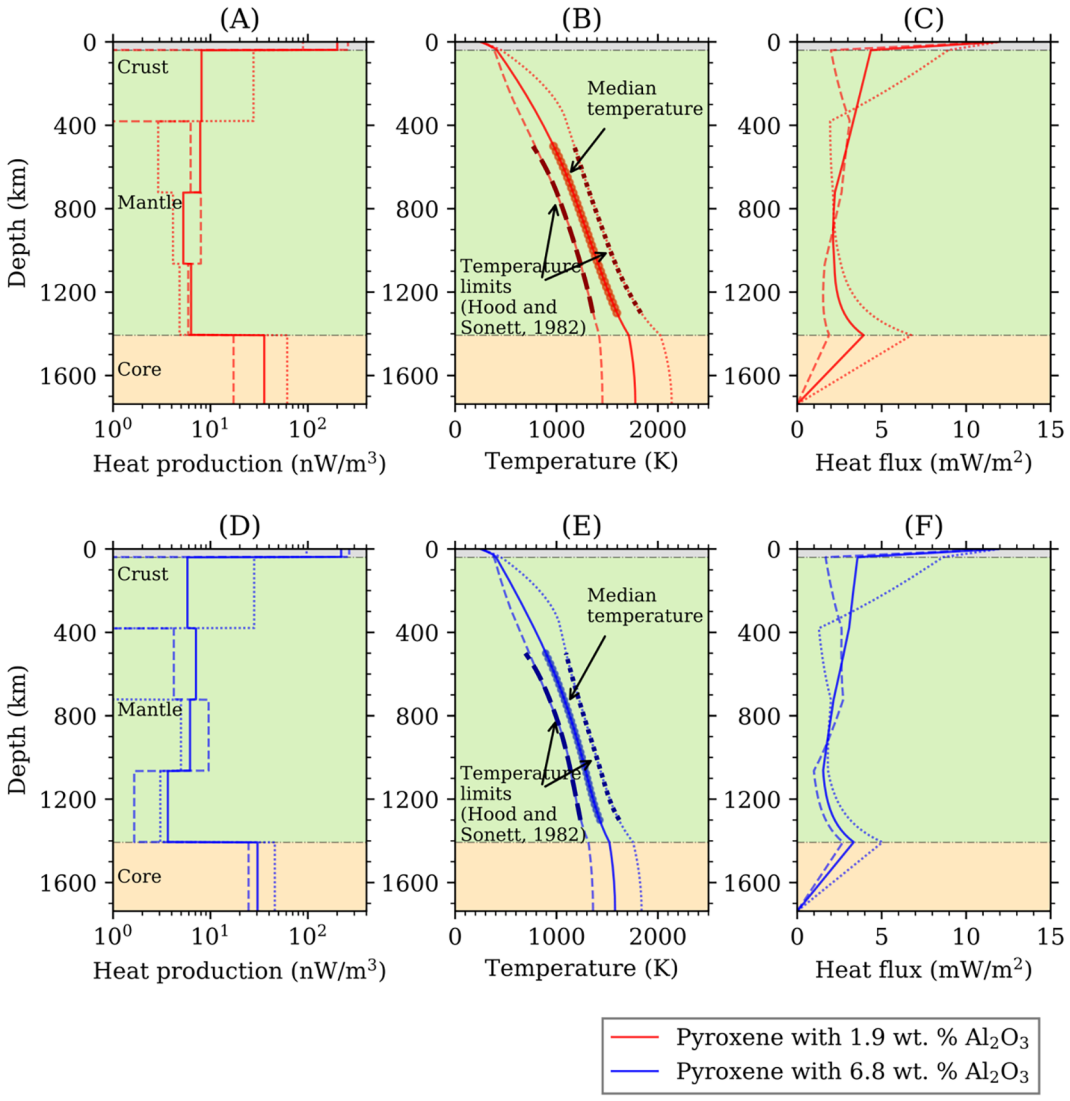

Fig. 5. The effects of the reference temperature variations on the inversion results for the mantle pyroxene with 1.9 wt% Al_2O_3 are shown in (A), (B) and (C) with red lines, and those for pyroxene with 6.8 wt% Al_2O_3 are shown in (D), (E) and (F) with blue lines. From left to right subfigures, the heat production, the temperature, and the heat flux along depth are shown. The dotted and dashed lines represent the upper and lower temperature limit and its inverted results, respectively. The minimum heat production in the top layer of the mantle are 1.1×10^{-7} nW/m^3 in (A), and 2.7×10^{-5} nW/m^3 in (D), which are too small to be shown in the figure. (For interpretation of the references to colour in this figure legend, the reader is referred to the web version of this article.)

reference temperatures have considerable effects on the inversion results.

5. Conclusions

This paper reports lunar interior temperature and heat production along depth by 1D forward modeling and geothermal inversion. The heat transfer of lunar interior is considered as a thermal conduction process. Particle swarm optimization is applied to calculate the inversion of heat production, which performs well and presents stable solutions.

According to our results, the lunar crust has the highest heat production of ~210 nW/m^3, while the lunar mantle has much lower values. The heat production of the lunar core lies between that of the crust and mantle and is near the mean heat production within the Moon. Geiss and Rossi (2013) presented a KREEP layer below the feldspathic crust. The KREEP layer is enriched in the radioactive elements derived from the mantle, for which the whole crust is expected to have a considerably high heat production. Our results support that the radioactive isotopes are highly enriched in the lunar crust from 0 to 40 km. In addition, although heat production decreases obviously below the lunar crust, there is an unpredicted high value within the core, indicating that the residual heat from lunar accretion or the abundances of the radioactive elements are likely to be substantial in the core and higher than the previous estimation in Toksöz et al., 1978.

Based on the assumption that the heat released by radioactive decay contributes to 80% of the total heat at present, we calculate the radioisotope abundance of uranium, thorium and potassium from the inversion results of heat production. Identical to the distribution of heat production, the radioisotopes mostly concentrate in the crust and are depleted in the mantle. The abundance of uranium in lunar crust is calculated to be 272 ppb, while that of thorium is 1007 ppb, which are in accordance with the average observations of Yamashita et al. (2010).

According to Weiss and Tikoo (2014), the intensity and longevity of the lunar dynamo depend on the heat flux at the core-mantle boundary. Core convection requires that the heat flux at the core-mantle boundary exceeds the core adiabat heat flux (between 2 and 10 mW/m^2). Our calculated heat flux has a low value of ~3.5 mW/m^2 in the range for the lunar core adiabatic process, suggesting that core convection probably has been greatly weakened.

Acknowledgements

This research is supported by the College Students' Innovation and Entrepreneurship Project under Grant No. 201711415081. And S. Yao is also supported by the Fundamental Research Funds for the Central Universities.

Appendix A

The spherical coordinates (r, θ, φ) are established with the origin located at the center of the Moon. The physical parameters of the lunar interior are considered to be isotropic. Therefore, the radius r is the only coordinate that needs to be considered. Since the moon has already cooled, the inner temperature field can be considered constant over time on a short time scale, which means $\partial T/\partial t \approx 0$ in Eq. (1). Hence, Eq. (1) can be written

$$A(r) = \frac{1}{r^2}\frac{\mathrm{d}}{\mathrm{d}r}(r^2 q(r)), \tag{8}$$

which can be integrated to give

$$q(r_1) = \frac{1}{r_1^2}\int_0^{r_1} A(r) r^2 \mathrm{d}r, \quad 0 \le r_1 \le R, \tag{9}$$

where $q(0) = 0$, and R is the radius of the moon. Thus, knowing the heat production of each layer, we can determine the heat flux from Eq. (9).

The discrete form of the heat flux in Eq. (9) is

$$\begin{aligned} q_{n+1} &= \frac{r_n^2}{r_{n+1}^2} q_n + \frac{r_{n+1}^3 - r_n^3}{3 r_{n+1}^2} A_{n+1}, \quad n = 0, 1, 2, \cdots \\ q_0 &= 0, \quad r_n = n \ \text{km}. \end{aligned} \tag{10}$$

where q_0 is the heat flux at the center of the Moon, A is the heat production per unit volume, and n is the ordinal number.

Integrating Eq. (2), we have

$$T(r_1) = T(0) - \int_0^{r_1} \frac{q(r)}{\lambda(r)}\mathrm{d}r, \tag{11}$$

where $T(0)$ is the central temperature of the moon. However, it is difficult to measure or evaluate $T(0)$ directly. We substitute $r_1 = R$ into Eq. (10) and obtain

$$T(0) = T_s + \int_0^{R} \frac{q(r)}{\lambda(r)}\mathrm{d}r, \tag{12}$$

where T_s is the subsurface temperature and is much easier to estimate than the central temperature.

Using Eqs. (10)–(12), we obtain

$$T(r_1) = T_s + \int_0^{R} \frac{\int_0^{r} A(r) r^2 \mathrm{d}r}{\lambda(r) r^2}\mathrm{d}r - \int_0^{r_1} \frac{\int_0^{r} A(r) r^2 \mathrm{d}r}{\lambda(r) r^2}\mathrm{d}r, \quad 0 \le r_1 \le R,$$

i.e., Eq. (3) shown in Section 2.1. We can also write it in discrete form:

$$\begin{aligned} T_{n+1} &= T_n - \frac{q_n}{\lambda_n}(r_{n+1} - r_n), \quad n = 0, 1, 2, \cdots \\ T_0 &= T_s + \textstyle\sum_{n=0} \frac{q_n}{\lambda_n}(r_{n+1} - r_n), \\ r_n &= n \ \text{km}. \end{aligned} \tag{13}$$

where T_0 is the temperature at the center of the moon, λ is the thermal conductivity, and n is the ordinal number.

On the other hand, if we substitute Eq. (2) into Eq. (1), we have

$$A(r) = \frac{1}{r^2}\frac{\mathrm{d}}{\mathrm{d}r}\left(-\lambda(r) r^2 \cdot \frac{\mathrm{d}T}{\mathrm{d}r}\right).$$

In each layer, $\mathrm{d}\lambda(r)/\mathrm{d}r$ equals zero. In this case, we write

$$A(r) = -\lambda(r)\left(\frac{2}{r}\frac{\mathrm{d}T}{\mathrm{d}r} + \frac{\mathrm{d}^2 T}{\mathrm{d}r^2}\right). \tag{14}$$

With Eq. (14), the heat production can also be calculated directly from temperature, which is shown as the red lines in Fig. 2. However, direct calculation is not recommended because it is rather sensitive to the temperature, and the results may have a large disturbance with a rough temperature profile.

References

Apollo 15 Preliminary Examination Team, 1972. The Apollo 15 lunar samples: a preliminary description. Science 363–375.

Apollo 16 Preliminary Examination Team, 1973. The Apollo 16 lunar samples: petrographic and chemical description. Science 23–34.

Branlund, J.M., Hofmeister, A.M., 2012. Heat transfer in plagioclase feldspars. Am. Mineral. 97 (7), 1145–1154.

Clark, R.S., Keith, J.E., 1973. Determination of natural and cosmic ray induced radionuclides in Apollo 16 lunar samples. In: Lunar and Planetary Science Conference Proceedings, vol. 4, p. 2105.

Clerc, M., Kennedy, J., 2002. The particle swarm-explosion, stability, and convergence in a multidimensional complex space. IEEE Trans. Evol. Comput. 6 (1), 58–73.

Duba, A., Heard, H.C., Schock, R.N., 1976. Electrical conductivity of orthopyroxene to 1400° and the resulting selenotherm. In: Proc. Lunar Sci. Conf. 7th, pp. 3173–3181.

Gagnepain-Beyneix, J., Lognonné, P., Chenet, H., Lombardi, D., Spohn, T., 2006. A seismic model of the lunar mantle and constraints on temperature and mineralogy. Phys. Earth Planet. In. 159 (3–4), 140–166.

Geiss, J., Rossi, A.P., 2013. On the chronology of lunar origin and evolution. Astron. Astrophys. Rev. 21 (1), 68.

Hood, L.L., Sonett, C.P., 1982. Limits on the lunar temperature profile. Geophys. Res. Lett.

9 (1), 37–40.
Khan, A., Mosegaard, K., Williams, J.G., Lognonné, P., 2004. Does the Moon possess a molten core? Probing the deep lunar interior using results from LLR and Lunar Prospector. J. Geophys. Res.: Planets 109 (E9).
Keldysh, M.V., 1977. Venus exploration with the Venera 9 and Venera 10 spacecraft. Icarus 30 (4), 605–625.
Kennedy, J., Eberhart, R.C., 1995. Particle swarm optimization. In: Proceedings of the 1995 IEEE International Conference on Neural Networks (Perth, Australia), pp. 1942–1948.
Langseth, M.G., Keihm, S.J., Peters, K., 1976. Revised lunar heat-flow values. In: Lunar and Planetary Science Conference Proceedings, vol. 7, pp. 3143–3171.
Lognonné, P., Gagnepain-Beyneix, J., Chenet, H., 2003. A new seismic model of the Moon: implications for structure, thermal evolution and formation of the Moon. Earth Planet. Sci. Lett. 211 (1–2), 27–44.
Metzger, A.E., Trombka, J.I., Peterson, L.E., Reedy, R.C., Arnold, J.R., 1972. A first look at the lunar orbital gamma ray data. In: Proc. Third Lunar Sci. Conf., vol. 3. MIT Press.
Paige, D.A., Siegler, M.A., Zhang, J.A., et al., 2010. Diviner lunar radiometer observations of cold traps in the moon's south polar region. Science 330, 479–482.
Poli, R., Kennedy, J., Blackwell, T., 2007. Particle swarm optimization. Swarm Int. 1 (1), 33–57.
Sonett, C.P., Duba, A., 1975. Lunar temperature and global heat flux from laboratory electrical conductivity and lunar magnetometer data. Nature 258 (5531), 118.
Sonett, C.P., 1982. Electromagnetic induction in the Moon. Rev. Geophys. 20 (3), 411–455.
Sanloup, C., Guyot, F., Gillet, P., Fiquet, G., Mezouar, M., Martinez, I., 2000. Density measurements of liquid Fe-S alloys at high-pressure. Geophys. Res. Lett. 27 (6), 811–814.
Siegler, M.A., Smrekar, S.E., 2014. Lunar heat flow: regional prospective of the Apollo landing sites. J. Geophys. Res.: Planets 119 (1), 47–63.
Tatsumoto, M., Knight, R.J., Allegre, C.J., 1973. Time differences in the formation of meteorites as determined from the ratio of lead-207 to lead-206. Science 180 (4092), 1279–1283.
Toksöz, M.N., Hsui, A.T., Johnston, D.J., 1978. Thermal evolutions of the terrestrial planets. Moon Planets 18 (3), 281–320.
Turcotte, D., Schubert, G., 2014. Geodynamics. Cambridge University Press.
Vasavada, A.R., Paige, D.A., Wood, S.E., 1999. Near-surface temperatures on Mercury and the Moon and the stability of polar ice deposits. Icarus 141 (2), 179–193.
Wang, H., Mighani, S., Weiss, B.P., Shuster, D.L., Hodges, K.V., 2017. Lifetime of the lunar dynamo constrained by young apollo returned breccias 15015 and 15465. In: Lunar and Planetary Science Conference, vol. 48.
Warren, P.H., Wasson, J.T., 1979. The origin of KREEP. Rev. Geophys. 17 (1), 73–88.
Warren, P.H., Rasmussen, K.L., 1987. Megaregolith insulation, internal temperatures, and bulk uranium content of the Moon. J. Geophys. Res.: Solid Earth 92 (B5), 3453–3465.
Weber, R.C., Lin, P.Y., Garnero, E.J., Williams, Q., Lognonne, P., 2011. Seismic detection of the lunar core. Science 331 (6015), 309–312.
Wieczorek, M.A., Phillips, R.J., 2000. The "Procellarum KREEP Terrane": implications for mare volcanism and lunar evolution. J. Geophys. Res.: Planets 105 (E8), 20417–20430.
Weiss, B.P., Tikoo, S.M., 2014. The lunar dynamo. Science 346 (6214), 1246753.
Yamashita, N., Hasebe, N., Reedy, R.C., Kobayashi, S., Karouji, Y., Hareyama, M., Shibamura, E., Kobayashi, M.N., Okudaira, O., d'Uston, C., Gasnault, O., 2010. Uranium on the moon: global distribution and U/Th ratio. Geophys. Res. Lett. 37 (10).